Mechatronics 118 (2026) 103526

Contents lists available at ScienceDirect

Mechatronics

journal homepage: www.elsevier.com/locate/mechatronics

Robust DOB design for asymmetric LPV hybrid gantry systems based on mode decomposition and nominal model selection☆,☆☆

Hanul Jung [a,1], Jegwon Yoon [b,1], Taejune Kong [b], Sehoon Oh [b,*]

[a] Mobility AI Convergence Research Section, ETRI, Daegu, 42994, Republic of Korea
[b] Department of Robotics and Mechatronics Engineering, DGIST, Daegu, 42988, Republic of Korea

ARTICLE INFO

Keywords:
Hybrid gantry stage
Linear parameter-varying systems
Disturbance observer
Mode decomposition
Robust stability

ABSTRACT

This paper presents a formalized framework for the design and verification of a disturbance observer (DOB) applied to a hybrid gantry stage with actuator asymmetry and payload-dependent LPV characteristics. The system consists of a rigid actuator and a series elastic actuator (SEA) arranged in parallel along the Y-axis, and an X-axis actuator that modifies payload distribution. Four payload configurations are considered, and frequency responses are analyzed to characterize mechanical coupling via Relative Gain Array (RGA). Canonical Polyadic Decomposition (CPD) is applied to derive transformation matrices for dynamic decoupling. The procedure sequentially integrates nominal model selection and DOB bandwidth determination in the transformed coordinates, followed by robust stability validation under varying operating conditions. The proposed framework provides a structured design procedure for LTI-based DOB implementation in asymmetric LPV MIMO systems.

1. Introduction

Gantry stages are widely used for precise planar motion control in semiconductor lithography, CNC machining, and medical imaging [1,2]. Rigid actuators provide high accuracy and repeatability, but the capability for force sensing and impact absorption required in industrial environments is limited.

Hybrid configurations combining a rigid actuator (RA) and a series elastic actuator (SEA) have been studied to achieve accurate position control, disturbance rejection, and compliance [3]. Mechanical compliance is essential for safety in interaction-aware systems. However, the system dynamics vary with the payload position and distribution, resulting in LPV behavior [4,5]. This variation requires advanced control strategies, but the deficiency of a systematic nominal model selection under LPV conditions restricts the use of conventional robust control methods.

Various LPV model-based control methods have been proposed to ensure stability and performance under parameter variations. Model Predictive Control (MPC) has been applied to LPV systems to explicitly handle constraints, with min–max optimization [6] and constraint tightening [7] used for robust design. LPV modeling has been applied to drill pipe dynamics with gain-scheduled control for vibration suppression and torque tracking [8]. $\mathcal{H}_\infty$ control has also been synthesized using frequency response data and norm-based criteria [9]. Nevertheless, most studies do not address dynamic interaction and decoupling in asymmetric LPV MIMO systems.

Tensor decomposition and Relative Gain Array (RGA) have been widely used for dynamic decoupling in MIMO systems. RGA quantifies input–output coupling and assists pairing [10]. SVD/modal decompositions can diagonalize the plant at each frequency, but the associated transforms are frequency-dependent and typically lead to an increase in model order when a single fixed-coordinate realization is required, which is not aligned with the LTI nominal-model-based DOB setting [11,12]. CPD extracts dominant modes from multidimensional FRFs [13] and provides an approximately frequency-invariant transform suitable for DOB design.

☆ This work was supported by Electronics and Telecommunications Research Institute, South Korea (ETRI) grant funded by the Korean government [26ZD1150, Advancement and Commercialization of Daegu-Gyeongbuk Regional Strategic Industries (Robots, Mobility, AI, Medical, etc.)], by the Basic Science Research Program through the National Research Foundation of Korea (NRF) funded by the Ministry of Education (RS-2025-25420118), and by the Institute of Information & Communications Technology Planning & Evaluation(IITP) grant funded by the Korea government(MSIT) (No.RS-2025-02219277, AI Star Fellowship Support (DGIST)).

☆☆ This paper was recommended for publication by Associate Editor Tom Oomen.

* Corresponding author.
E-mail addresses: hanul@etri.re.kr (H. Jung), sehoon@dgist.ac.kr (S. Oh).

[1] These authors contributed equally to this work.

https://doi.org/10.1016/j.mechatronics.2026.103526
Received 23 July 2025; Received in revised form 4 March 2026; Accepted 10 April 2026
Available online 25 April 2026

Disturbance observers (DOB) have been widely applied in SISO systems for disturbance and uncertainty compensation. In MIMO systems, centralized and decentralized DOBs, and static decoupling with channel-wise observers [14–16], have been investigated. Recently, LPV-based disturbance rejection schemes have also been explored in hybrid isolation platforms [17]. However, for asymmetric LPV MIMO gantry stages, the procedure that connects FRF/RGA-based coupling analysis, CPD-based dynamics decomposition, nominal model selection under payload variations, and frequency-domain robust stability verification is not clearly established [18]. This work presents a concise procedure: coupling characteristics are analyzed using measured FRFs/RGA, frequency-invariant transforms are obtained via CPD-based dynamics decomposition, a nominal model is selected from the transformed FRFs, and robust stability is verified over the design band by a small-gain condition that links normalized uncertainty and Q-filter bandwidth. The proposed procedure is formulated as a frozen-parameter FRF-based guideline, and its applicability is restricted to frequency ranges where diagonal dominance and approximate decoupling are verified.

Therefore, a DOB design and verification framework is established for a hybrid gantry stage with actuator asymmetry and payload-dependent LPV dynamics. Four payload conditions are considered, measured FRFs are used for coupling analysis and CPD-based decoupling, and the nominal model and Q-filter bandwidth are determined using a frequency-domain robust stability condition. Experiments confirm robust stability when the nominal model and Q-filter bandwidth are appropriately selected.

In summary, the main contributions of this study are threefold: (1) Coupling characteristics are analyzed in the frequency domain using measured FRFs/RGA, and CPD-based dynamics decomposition is performed to obtain frequency-invariant transforms for decoupling. (2) Candidate operating conditions are compared in the decoupled coordinates, and a nominal model is selected from the transformed FRFs under payload variations. (3) Robust stability of the DOB-based decoupling control is analyzed in the frequency domain using a small-gain condition that links the nominal model, normalized uncertainty, and Q-filter bandwidth.

2. Problem formulation

2.1. Asymmetric linear parameter varying gantry stage

The dual-drive gantry in this study uses an asymmetric hybrid actuation, in which the left Y-axis is driven by a rigid actuator (RA) and the right Y-axis by a reaction-force-sensing series elastic actuator (RFSEA) [19], as in Fig. 1. The parameters m_1, m_2, m_3, m_{cb}, and J_α denote the actuator/crossbeam masses and the crossbeam inertia. The actuator outputs are y_1, y_2, and x_3. The inputs F_1, F_2, and T_t act along the Y-axis, and the torque is written as an equivalent force $F_t = T_t/l_{cb}$.

The detailed physical configuration of the hybrid gantry system is presented in Fig. 2, where the actuator arrangement and payload position that define the asymmetric structure are clearly illustrated. Fig. 2 clarifies the relationship between the analytical model and the experimental system. This hybrid composition, rigid and elastic, results in asymmetric dynamics. Variation of the payload position changes mass and inertia distributions, which causes the system to operate as an LPV system.

The crossbeam couples the Y-axis actuators. The scheduling variable $\rho(t)$ (the X-axis position x_3 in Fig. 1) affects the crossbeam and the parallel actuators, modeled by $P_{cb}(s,\rho)$, $P_r(s,\rho)$, and $P_l(s,\rho)$ in Fig. 3.

The X-axis actuator position x_3, shown in Fig. 1, is defined as the scheduling variable $\rho \in [0, l_{cb}]$, where l_{cb} denotes the crossbeam length. The Y-axis outputs y_1 and y_2 are determined by the input forces F_1 and F_2, and the system is modeled as a two-input two-output structure influenced by the scheduling variable, as shown in Fig. 3.

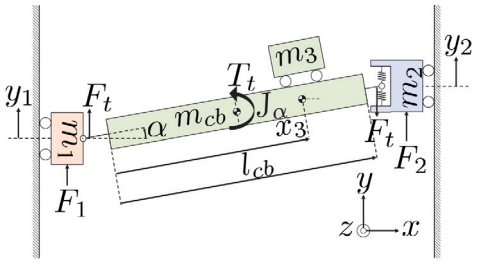

Fig. 1. Schematic of the hybrid dual-drive gantry stage with asymmetric actuation.

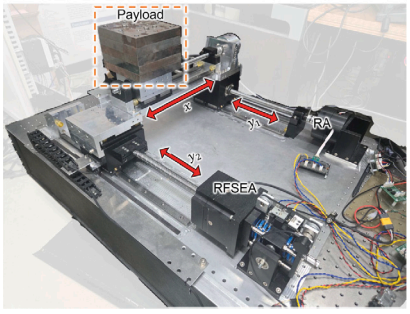

Fig. 2. Hybrid gantry stage with RA, RFSEA, and movable payload on the X-axis actuator.

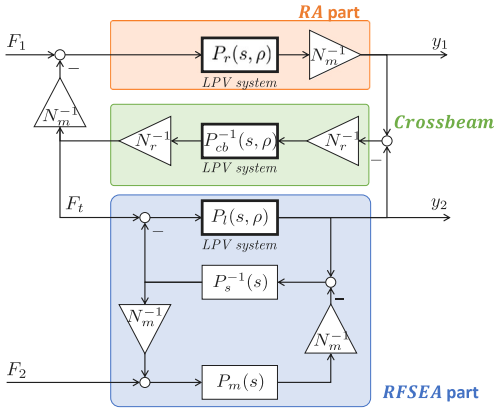

Fig. 3. Block diagram of the hybrid gantry stage represented as an LPV system.

The RFSEA is represented by $P_m(s)$, $P_s(s)$, and $P_l(s,\rho)$, and the RA/crossbeam by $P_r(s,\rho)$ and $P_{cb}(s,\rho)$. The Y-axis outputs $[y_1, y_2]^T$ are determined by $[F_1, F_2]^T$ through the TITO plant $\boldsymbol{P}(s,\rho)$ in (2). The element transfer functions are given in (3)–(6) with $P_{rf} = (P_m + P_l + P_s)^{-1}(P_l P_m + P_l P_s)$.

$$P_r(s) = \frac{1}{M_r(\rho)s^2}, \qquad P_{cb}(s) = \frac{1}{J_\alpha(\rho)s^2}, \tag{1}$$
$$P_m(s) = \frac{1}{M_m s^2}, \qquad P_s(s) = \frac{1}{M_s s^2}, \qquad P_l(s) = \frac{1}{M_l(\rho)s^2},$$

where $M_r(\rho)$, $M_l(\rho)$, and $J_\alpha(\rho)$ represent the equivalent mass and inertia of the RA, RFSEA, and crossbeam, respectively, and vary with the scheduling variable $\rho(t)$. In contrast, M_m and M_s denote the fixed masses of the motor and spring within the RFSEA.

Therefore, the system is expressed as a TITO plant $\boldsymbol{P}(s,\rho)$.

$$\begin{bmatrix} y_1 \\ y_2 \end{bmatrix} = \boldsymbol{P}(s,\rho) \begin{bmatrix} F_1 \\ F_2 \end{bmatrix} = \begin{bmatrix} P_{F_1\to y_1}(s,\rho) & P_{F_2\to y_1}(s,\rho) \\ P_{F_1\to y_2}(s,\rho) & P_{F_2\to y_2}(s,\rho) \end{bmatrix} \begin{bmatrix} F_1 \\ F_2 \end{bmatrix}, \tag{2}$$

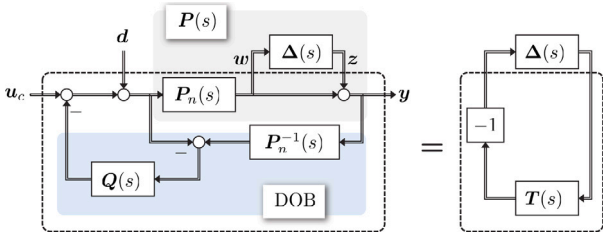

Fig. 4. Equivalent block diagram of the disturbance observer for robust stability analysis.

Each element of the transfer function matrix is given as follows:

$$P_{F_1\to y_1}(s,\rho)=\frac{P_rP_{cb}+P_rP_{rf}}{P_r+P_{rf}+P_{cb}}, \tag{3}$$

$$P_{F_1\to y_2}(s,\rho)=\frac{P_rP_{rf}}{P_r+P_{rf}+P_{cb}}, \tag{4}$$

$$P_{F_2\to y_1}(s,\rho)=\frac{P_mP_l}{P_lP_m+P_lP_s}\frac{P_rP_{rf}}{P_r+P_{rf}+P_{cb}}, \tag{5}$$

$$P_{F_2\to y_2}(s,\rho)=\frac{P_mP_l}{P_lP_m+P_lP_s}\frac{P_{rf}P_{cb}+P_rP_{rf}}{P_r+P_{rf}+P_{cb}}, \tag{6}$$

where $P_{rf}=(P_m+P_l+P_s)^{-1}(P_lP_m+P_lP_s)$ represents the transfer function from the input force F_t to the output y_2 in the RFSEA. Although expressed in a transfer-function form, the model represents the dominant linear dynamics identified from measured FRFs and serves as the basis for robust DOB design. The plant exhibits asymmetric LPV MIMO characteristics, which should be reflected in controller design.

2.2. Robust stability of disturbance observer in MIMO system

In industrial applications, considerable efforts have been made to design robust controllers against disturbances. The DOB is widely used for disturbance rejection and model uncertainty compensation, mainly in SISO systems. However, in MIMO systems, mechanical coupling complicates the direct application of conventional SISO DOB structures.

The left side of Fig. 4 shows the MIMO DOB structure, where $\boldsymbol{P}(s)$, $\boldsymbol{P}_n(s)$, and $\boldsymbol{Q}(s)$ denote the plant, diagonal nominal model, and bandwidth-setting Q-filter, respectively. u_c, d, and y are the control input, disturbance, and measured output, while $\hat{d}$ and $\hat{u}$ represent the estimated disturbance and control input.

The DOB compensates for lumped disturbance, including friction, external forces, and model errors, and achieves robust performance under model uncertainties. The closed-loop transfer function of the DOB is given as follows:

$$\boldsymbol{P}_{u_c\to y}(s)=\left[\boldsymbol{I}-\boldsymbol{Q}(s)+\boldsymbol{Q}(s)\boldsymbol{P}_n^{-1}(s)\boldsymbol{P}(s)\right]^{-1}\boldsymbol{P}(s), \tag{7}$$

$$\boldsymbol{P}_{d\to y}(s)=\left[\boldsymbol{I}-\boldsymbol{Q}(s)+\boldsymbol{Q}(s)\boldsymbol{P}_n^{-1}(s)\boldsymbol{P}(s)\right]^{-1}(\boldsymbol{I}-\boldsymbol{Q}(s))\,\boldsymbol{P}(s), \tag{8}$$

The Q-filter is generally designed as a low-pass filter. When $\boldsymbol{Q}(s)\approx 1$ in the low-frequency range, the closed-loop transfer function of the DOB becomes:

$$\boldsymbol{P}_{u_c\to y}(s)=\boldsymbol{P}_n(s), \tag{9}$$

$$\boldsymbol{P}_{d\to y}(s)=0, \tag{10}$$

(9) and (10) indicate that the DOB generates a response normalized by the nominal model and performs disturbance rejection.

However, the DOB is sensitive to the accuracy of $\boldsymbol{P}_n(s)$ and $\boldsymbol{Q}(s)$, and the influence of model uncertainty and DOB bandwidth on system stability should therefore be analyzed prior to implementation. Robustness is defined as the preservation of closed-loop stability within the DOB design bandwidth under payload-induced variations relative to the selected nominal model.

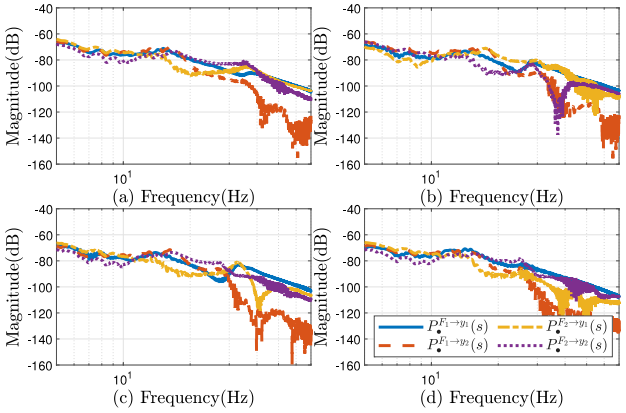

Fig. 5. Measured FRFs of the hybrid gantry stage under different payload conditions before CPD-based decoupling. (a): no additional mass, (b): mass on RA side, (c): mass at crossbeam center, (d): mass on SEA side.

The right side of Fig. 4 shows the framework for analyzing DOB robust stability. The system is expressed as a closed-loop $\boldsymbol{T}_{z\to w}(s)$ from input z to output w with model uncertainty $\boldsymbol{\Delta}(s)$, where $\boldsymbol{P}(s)=\boldsymbol{P}_n(s)[\boldsymbol{I}+\boldsymbol{\Delta}(s)]$ and $\boldsymbol{\Delta}(s)=\boldsymbol{P}_n^{-1}(s)[\boldsymbol{P}(s)-\boldsymbol{P}_n(s)]$.

The robust stability of the DOB with respect to the nominal model is assessed, and robust stability against model uncertainty $\boldsymbol{\Delta}(s)$ is ensured if the following condition is satisfied:

$$\left\|\boldsymbol{\Delta}(j\omega)\boldsymbol{T}_{z\to w}(j\omega)\right\|_\infty<1, \tag{11}$$

where $\|\bullet\|_\infty$ is the $\mathcal{H}_\infty$-norm, and $\boldsymbol{T}_{z\to w}(j\omega)$ denotes the closed-loop DOB system in the s-domain, defined as:

$$\boldsymbol{T}_{z\to w}(s)=\left[\boldsymbol{I}+\left(\boldsymbol{P}_n(s)(\boldsymbol{I}-\boldsymbol{Q}(s))^{-1}\boldsymbol{Q}(s)\boldsymbol{P}_n^{-1}(s)\right)^{-1}\right]^{-1}. \tag{12}$$

Additionally, (11) links DOB bandwidth and model uncertainty, which motivates a conservative nominal-model and Q-filter selection.

In practice, the DOB is combined with an outer feedback controller $\boldsymbol{C}_{fb}(s)$. The same small-gain framework applies by replacing $\boldsymbol{T}_{z\to w}(j\omega)$ in (11) with the corresponding closed-loop interconnection as

$$\boldsymbol{T}^{fb}_{z\to w}(j\omega)=\left[\boldsymbol{Q}(j\omega)+\boldsymbol{P}_n(j\omega)\boldsymbol{C}_{fb}(j\omega)\right]\left[\boldsymbol{I}+\boldsymbol{P}_n(j\omega)\boldsymbol{C}_{fb}(j\omega)\right]^{-1}. \tag{13}$$

When the outer-loop bandwidth is lower than the DOB bandwidth, (11) provides a practical stability guideline for the closed-loop system.

3. Frequency response function based analysis of novel hybrid gantry stage

3.1. Frequency response analysis under operating conditions

This section characterizes resonance/coupling features from measured FRFs to support DOB design under asymmetric LPV dynamics (see Fig. 4).

In this experiment, FRFs are measured for outputs y_1 and y_2 under inputs F_1 and F_2 across four representative payload cases: RA end (ra), SEA end (se), crossbeam center (ce), and no additional mass (nm). The system exhibits LPV behavior with moderate dependence on payload position, and the four cases are chosen as corner conditions covering the operating range, where ρ is fixed and $\dot{\rho}=0$ during each FRF measurement. The FRFs are obtained under closed-loop position control using a Schroeder-phase multisine excitation applied to the commanded inputs, and the measured responses are ensemble-averaged after discarding the initial transient to improve repeatability of the estimated FRFs.

Fig. 5 shows FRFs for four payload conditions: $\boldsymbol{P}_{nm}$, $\boldsymbol{P}_{ra}$, $\boldsymbol{P}_{ce}$, and $\boldsymbol{P}_{se}$, corresponding to no mass, mass on the RA side, center, and SEA

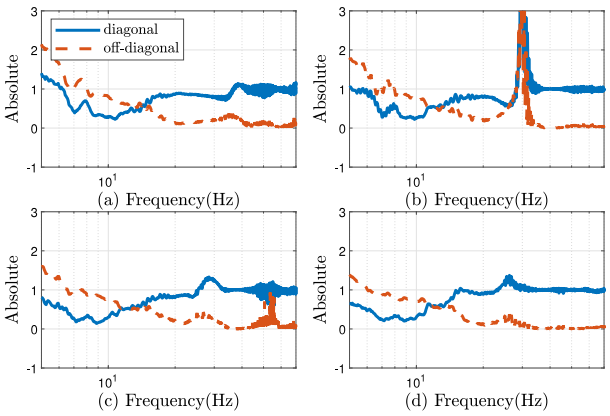

Fig. 6. RGA magnitude responses of the hybrid gantry stage under different payload conditions before CPD-based decoupling. (a): no additional mass, (b): mass on RA side, (c): mass at crossbeam center, (d): mass on SEA side.

side, respectively. Each line indicates the output response of y_1 or y_2 to F_1 or F_2.

All mass-added conditions ($\boldsymbol{P}_{ra}$, $\boldsymbol{P}_{ce}$, $\boldsymbol{P}_{se}$) consistently exhibit a lower resonance frequency in the second mode. This indicates that the increased system inertia affects higher-order dynamic modes significantly. In addition, the characteristics in (3)~(6) differ between F_1 and F_2 for the same output, revealing structural asymmetry and distinct RA/SEA-output interactions.

In the RA-side output response (y_1), resonance peaks are consistently observed across all conditions. $P_{\bullet}^{F_1\to y_1}$, associated with the rigid-body-like mode of the RA side, remains stable in both shape and frequency regardless of mass placement, reflecting the limited influence of added mass due to the high stiffness of the RA structure. In contrast, the SEA-side output response (y_2) exhibits noticeable anti-resonance behavior under several conditions, with the most significant depth and frequency sensitivity observed under the $\boldsymbol{P}_{se}$ condition. This indicates that the compliant SEA-side actuator exhibits increased sensitivity to changes in mass location.

These results experimentally demonstrate that the hybrid gantry stage features both structural asymmetry and input dependent dynamic behavior. Therefore, in the subsequent controller design, a nominal model selection strategy is essential, taking into account not only mechanical coupling but also the asymmetric characteristics of the system.

3.2. Coupling analysis and dynamic decomposition of hybrid gantry stage

The hybrid gantry stage is an asymmetric MIMO system with mechanical coupling. RGA analysis is performed based on the measured FRFs to quantify frequency-dependent interaction and to verify whether diagonal dominance holds within the design bandwidth [10].

The RGA for the system $\boldsymbol{P}_{\bullet}(j\omega)$ is defined as follows:

$$\boldsymbol{\Lambda}(j\omega) = \boldsymbol{P}_{\bullet}(j\omega) \circ \left(\boldsymbol{P}_{\bullet}^{-1}(j\omega)\right)^{T}, \tag{14}$$

where $\circ$ is the Hadamard product (element-wise multiplication). Diagonal dominance is assessed by the RGA, and the coupling level is quantified by:

$$\xi_{\mathrm{RGA}}(\omega) = \sum_{i} |\Lambda_{ii}(\omega) - 1| + \sum_{i\neq j} |\Lambda_{ij}(\omega)|. \tag{15}$$

A coupling level is regarded as acceptable within the design bandwidth $\Omega = [0, f_{\mathrm{DOB}}]$ when $\xi_{\mathrm{RGA}}(\omega) \le 0.5$, $|\Lambda_{ii}(\omega) - 1| \le 0.2$, and $|\Lambda_{ij}(\omega)| \le 0.2$.

Fig. 6 shows that the acceptance criterion is violated within the design bandwidth for all payload cases, and Table 2 confirms that

Table 1
Transformation matrices of CPD.

	$\boldsymbol{U}$	$\boldsymbol{V}$
$\{\boldsymbol{U},\boldsymbol{V}\}_{ra}$	[0.13, −0.06; 0.14, 0.04]	[7.80, −2.82; 6.01, 5.09]
$\{\boldsymbol{U},\boldsymbol{V}\}_{se}$	[0.15, −0.06; 0.16, 0.04]	[6.86, −3.55; 5.36, 3.36]
$\{\boldsymbol{U},\boldsymbol{V}\}_{ce}$	[0.13, −0.06; 0.13, 0.04]	[7.66, −3.50; 6.26, 5.00]
$\{\boldsymbol{U},\boldsymbol{V}\}_{nm}$	[0.20, −0.08; 0.18, 0.06]	[0.59, −2.13; 0.55, 4.11]

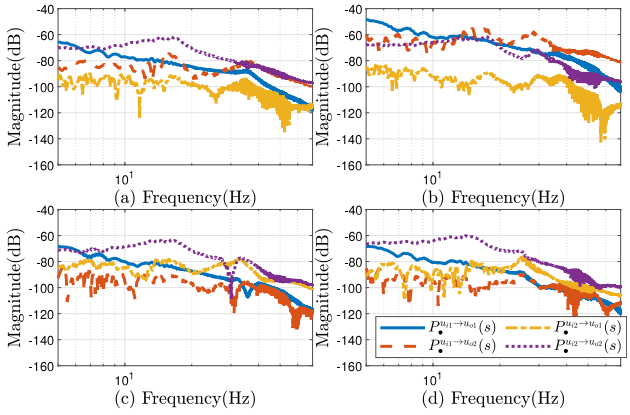

Fig. 7. Measured FRFs of the hybrid gantry stage under different payload conditions after CPD-based decoupling. (a) No additional mass, (b) Mass added on RA side, (c) Mass added at crossbeam center, (d) Mass added on SEA side.

diagonal dominance cannot be ensured without structural reconfiguration. Therefore, CPD is introduced to obtain an approximately diagonal representation suitable for DOB design.

The measured FRFs over inputs, outputs, and frequency points are arranged as a three-dimensional tensor, and CPD is applied to extract dominant mode components and to obtain frequency-invariant input/output transforms [13].

Therefore, CPD is applied to decompose the three-dimensional frequency response tensor into input/output transformations and frequency components [13], as follows:

$$\mathcal{T} = \sum_{r=1}^{R} u_r^1 \otimes u_r^2 \otimes \cdots \otimes u_r^{N_t} + \mathcal{E}, \tag{16}$$

where R is the target rank, N_t the tensor order, $\otimes$ the outer product, and $\mathcal{E}$ the error tensor. The CPD minimizes $\|\mathcal{E}\|_{\mathcal{F}}^2$ with respect to $u_r^{\bullet}$.

As a result, CPD enables the identification of dominant dynamic modes and facilitates controller design [11]. The resulting transformation matrices ($\boldsymbol{U}_{\blacksquare}$, $\boldsymbol{V}_{\blacksquare}$) are presented in Table 1.

Fig. 7 shows the frequency responses of the hybrid gantry stage after CPD-based decoupling. Each subplot corresponds to a payload condition: (a) no additional mass ($\boldsymbol{P}_{nm|nm}$), (b) mass on the RA side ($\boldsymbol{P}_{ra|ra}$), (c) mass at the crossbeam center ($\boldsymbol{P}_{ce|ce}$), and (d) mass on the SEA side ($\boldsymbol{P}_{se|se}$). In $\boldsymbol{P}_{\bullet|\blacksquare}$, $\bullet$ indicates the measurement condition and $\blacksquare$ the applied CPD transformation (e.g., $\boldsymbol{P}_{nm|ra}(s) = \boldsymbol{U}_{ra}^{-1}\boldsymbol{P}_{nm}(s)\boldsymbol{V}_{ra}^{-T}$). Each line represents an output response to a decoupled input.

Fig. 7 shows that CPD provides an approximately diagonal representation that preserves the modal resonance structure. For frequencies beyond ~20 Hz, magnitude crossover remains, which indicates residual coupling under strong asymmetry and motivates a bandwidth selection based on the RGA of the CPD-decoupled system.

Therefore, CPD is used to obtain practical decoupling coordinates, while the feasible bandwidth is finalized by the RGA-based acceptance criterion after CPD-based decoupling.

Fig. 8 presents the RGA magnitude responses after CPD-based decoupling. With the acceptance criterion $|\Lambda_{ii} - 1| \le 0.2$ and $|\Lambda_{ij}| \le 0.2$ over $\Omega = [0, f_{\mathrm{DOB}}]$, $\boldsymbol{P}_{nm|nm}$ satisfies the criterion up to ≈ 35 Hz, after which coupling increases as seen in Fig. 7.

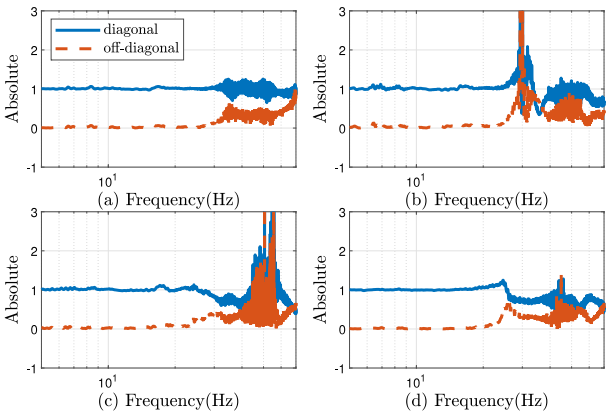

Fig. 8. RGA magnitude responses of the hybrid gantry stage under different payload conditions after CPD-based decoupling. (a) No additional mass (baseline), (b) Mass on RA side, (c) Mass at crossbeam center, (d) Mass on SEA side.

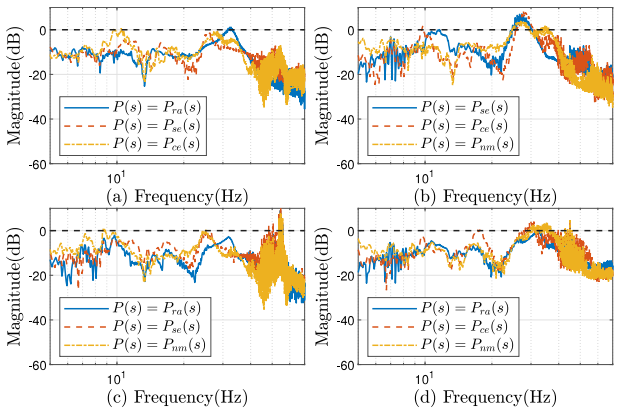

Fig. 9. Robust stability analysis using the non-decoupled frequency response, with $Q(s)$ including resonance dynamics (cutoff frequency: 35 Hz); (a) $P_n^{nm}(s)$, (b) $P_n^{ra}(s)$, (c) $P_n^{ce}(s)$, and (d) $P_n^{se}(s)$.

Table 2
Quantitative evaluation of RGA-based decoupling before and after CPD transformation. Acceptance conditions: $\xi_{RGA} \le 0.5$, $|\Lambda_{ii} - 1| \le 0.2$, $|\Lambda_{ij}| \le 0.2$.

Design band	Case	ξ_∞		Max $\lvert\Lambda_{ii} - 1\rvert$		Max $\lvert\Lambda_{ij}\rvert$	
		Before	After	Before	After	Before	After
~35 Hz	nm	5.10	0.39	0.78	0.06	2.14	0.15
	ra	19.54	11.64	4.43	2.56	5.34	3.26
	ce	3.67	1.13	0.86	0.18	1.60	0.42
	se	3.47	1.76	0.80	0.33	1.39	0.66
~20 Hz	nm	5.10	0.26	0.78	0.06	2.14	0.08
	ra	3.70	0.50	0.78	0.12	1.79	0.14
	ce	3.67	0.48	0.86	0.12	1.60	0.13
	se	3.47	0.33	0.80	0.08	1.39	0.08

When the design bandwidth is restricted to 20 Hz, the criterion is satisfied for all payload cases. The pass/fail summary over $\Omega = [0, 20]$ Hz and $\Omega = [0, 35]$ Hz is provided in Table 2, indicating that $\boldsymbol{P}_{nm|nm}$ is appropriate as the nominal-model basis within a 35 Hz target, while a 20 Hz design bandwidth ensures acceptable decoupling across all cases.

The RGA acceptance conditions define the valid DOB design bandwidth in a design-oriented manner, and if the criterion is not satisfied after CPD, the design is restricted to a smaller feasible bandwidth.

4. Disturbance observer design and robust stability analysis

4.1. Comparison condition for nominal model selection of disturbance observer

This section evaluates nominal-model selection and DOB bandwidth using the robust-stability condition under payload variations, including comparisons between non-decoupled and CPD-decoupled representations.

To elaborate on the robust stability analysis procedure, the decoupled case based on the nm condition is considered, and the following steps are followed.

1. The transformation matrices $\boldsymbol{U}_{nm}$ and $\boldsymbol{V}_{nm}$ obtained under ($\boldsymbol{P}_{nm}$) condition are defined.
2. The nominal model $\boldsymbol{P}_n^{nm}(s)$ is defined as the diagonal components of the CPD-decomposed no-load model: $\boldsymbol{P}_n^{nm}(s) = \mathrm{diag}\big(\boldsymbol{P}_{nm|nm}(s)\big)$
3. The actual system $\boldsymbol{P}(s)$ consists of the decoupled dynamics obtained using the nm-based transformation matrices under the three payload conditions: $\boldsymbol{P}_{\{ra,se,ce\}|nm}(s) := \boldsymbol{U}_{nm}^{-1}\,\boldsymbol{P}_{\{ra,se,ce\}}(s)\,\boldsymbol{V}_{nm}^{-T}$
4. Robust stability is evaluated by the worst-case small-gain cost over the LPV corner conditions:

$$J_k \triangleq \max_{\rho \neq k} \sup_{\omega \in [0, 2\pi f_{\mathrm{DOB}}]} 20\log_{10}\big(\bar{\sigma}\big(\boldsymbol{\Delta}(j\omega)\boldsymbol{T}_{z\to w}(j\omega)\big)\big), \tag{17}$$

and $J_k < 0$ dB ensures robust stability over $\Omega = [0, f_{\mathrm{DOB}}]$.

Sections 4.2 and 4.3 examine 35 Hz and 20 Hz, respectively. The bandwidths are chosen by inspecting the RGA index of the measured FRFs and selecting the maximum design band that does not exceed acceptance thresholds, resulting in approximately 35 Hz for the nm condition after CPD and a conservative 20 Hz that remains admissible across all payload conditions. Both settings respect the practical phase-lag bound of the Q-filter and preserve sufficient phase margin, including digital delays.

In addition, the RS formulation can be extended to a practical closed-loop configuration including an outer feedback controller, and the feasibility conclusion is preserved under the same nominal selection procedure.

4.2. Robust stability analysis based on nominal model and payload conditions

In this section, the DOB bandwidth is set to 35 Hz, and robust stability is evaluated by applying either the non-decoupled or the CPD-decoupled nominal model. This comparison provides an evaluation of the nominal model selection approach for the DOB.

The four subplots in Figs. 9 and 10 correspond to different choices of nominal models used in the disturbance observer design: top-left: nm (no additional mass), top-right: *ra* (mass attached to the rigid actuator), bottom-left: *ce* (mass attached at the center), and bottom-right: *se* (mass attached to the SEA). Each subplot shows the actual system responses under three different payload conditions. The black dashed line indicates the robust stability threshold (0 dB), and the responses are required to remain below this line across the entire frequency range to satisfy the robust stability condition.

Fig. 9 shows the robust stability based on the non-decoupled system. In all conditions, frequency regions exceeding 0 dB are observed. This result implies that, in an asymmetric LPV system, the use of a conventional nominal model without dynamic decoupling makes it difficult to achieve robust stability due to the influence of resonance dynamics. Therefore, it becomes fundamentally difficult to design a DOB whose bandwidth includes resonant dynamics when using the non-decoupled model.

Fig. 10 shows the robust stability results when the DOB is designed based on the CPD-decoupled model. When $\boldsymbol{P}_n^{nm}(s)$ is used as the nominal

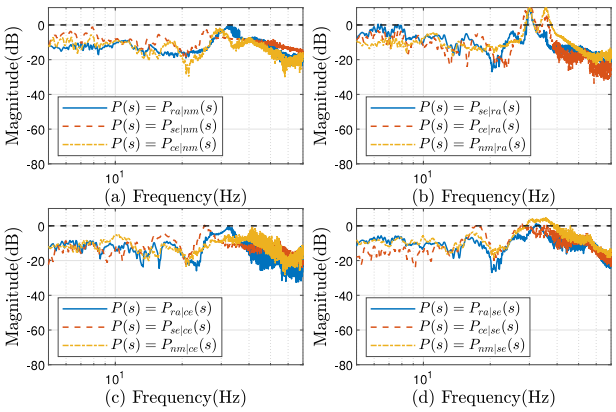

Fig. 10. Robust stability analysis using the CPD-decoupled frequency response, with $Q(s)$ including resonance dynamics (cutoff frequency: 35 Hz); (a) $\boldsymbol{P}_n^{nm}(s)$, (b) $\boldsymbol{P}_n^{ra}(s)$, (c) $\boldsymbol{P}_n^{ce}(s)$, and (d) $\boldsymbol{P}_n^{se}(s)$.

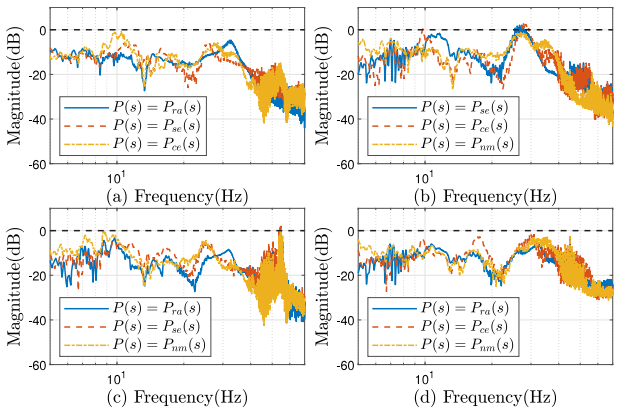

Fig. 11. Robust stability analysis using the non-decoupled frequency response, with $Q(s)$ excluding resonance dynamics (cutoff frequency: 20 Hz); (a) $\boldsymbol{P}_n^{nm}(s)$, (b) $\boldsymbol{P}_n^{ra}(s)$, (c) $\boldsymbol{P}_n^{ce}(s)$, and (d) $\boldsymbol{P}_n^{se}(s)$.

model, as shown in Fig. 10(a), all payload conditions remain below 0 dB, and robust stability is satisfied. In contrast, when $\boldsymbol{P}_n^{ra}(s)$, $\boldsymbol{P}_n^{ce}(s)$, or $\boldsymbol{P}_n^{se}(s)$ is applied in Figs. 10 (b)~(d), responses exceeding 0 dB are observed in all payload conditions.

These results imply that CPD-based decoupling is advantageous for achieving sufficient DOB bandwidth from the perspective of robust st ability. In particular, for asymmetric MIMO systems, using the no-load (nm) condition as the nominal model is considered appropriate. Although CPD is applied, the choice of nominal model has a significant impact on robust stability. In addition, the robust stability evaluation aims to select a nominal model, not to satisfy all cases simultaneously, and the evaluation is used to select a feasible nominal candidate. For a selected nominal model, the small-gain condition must hold for all remaining payload cases over the design band. In this context, the no-load (nm) condition is a reasonable and effective choice because the no-load case places resonances higher and reduces asymmetric coupling, leading to smaller normalized uncertainty under the same Q-filter and a consistently larger robust-stability margin. The resulting worst-case values J_k are summarized in Table 3 for a compact comparison among nominal candidates. At f_{DOB} = 35 Hz, the nm-based nominal model is the only candidate that satisfies the robust-stability condition after CPD, enabling the highest admissible DOB bandwidth among the candidates.

4.3. Robust stability analysis based on bandwidth and payload conditions

In this section, robust stability is analyzed with the DOB cutoff frequency set to 20 Hz to suppress resonance dynamics.

Fig. 11 shows the robust stability results when the DOB is designed based on the FRF of the non-decoupled system. Robust stability is satisfied when $\boldsymbol{P}_n^{nm}(s)$ or $\boldsymbol{P}_n^{se}(s)$ is used, as all payload conditions remain below 0 dB. In contrast, for the other cases, certain frequency regions exceed 0 dB. These results indicate that reducing the DOB bandwidth can help achieve robust stability under specific conditions. However, the choice of nominal model has a significant influence on stability.

Fig. 12 shows the case where the DOB is designed using the CPD-decoupled model, and the analysis is conducted based on the same four nominal model conditions. The cases based on $\boldsymbol{P}_n^{ce}(s)$ and $\boldsymbol{P}_n^{se}(s)$ satisfy the robust stability condition across the entire frequency range. However, when $\boldsymbol{P}_n^{ra}(s)$ is used, certain responses approach or exceed 0 dB under specific conditions. In this case, robust stability is not fully achieved.

These results indicate that reducing the DOB bandwidth can be effective in ensuring robust stability, and confirm that CPD-based models can improve stability across various payload conditions. However, the limited bandwidth can degrade disturbance rejection performance in the high-frequency range, highlighting the need to consider the trade-off between control performance and robust stability in the design process. Table 3 provides a worst-case robustness summary of Figs. 9–12 via J_k over $\Omega = [0, f_{\mathrm{DOB}}]$ and the LPV corner plants.

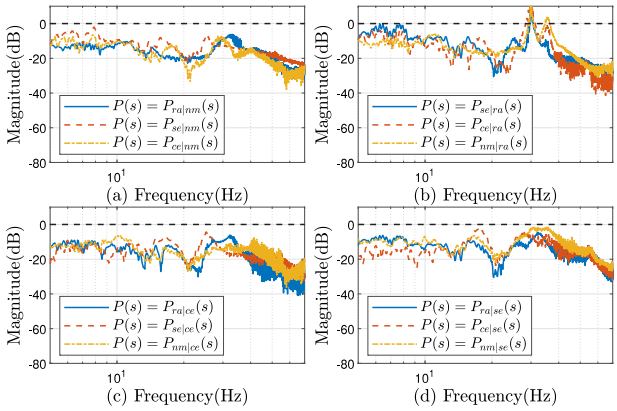

Fig. 12. Robust stability analysis using the CPD-decoupled frequency response, with $Q(s)$ excluding resonance dynamics (cutoff frequency: 20 Hz); (a) $\boldsymbol{P}_n^{nm}(s)$, (b) $\boldsymbol{P}_n^{ra}(s)$, (c) $\boldsymbol{P}_n^{ce}(s)$, and (d) $\boldsymbol{P}_n^{se}(s)$.

Table 3
Worst-case robustness cost J_k over $\Omega = [0, f_{\mathrm{DOB}}]$ evaluated over the LPV corner conditions.

k	f_{DOB} = 20 Hz		f_{DOB} = 35 Hz	
	J_k (Before)	J_k (After)	J_k (Before)	J_k (After)
nm	−0.728	−1.947	1.180	−0.299
ra	0.529	−0.079	8.060	29.835
ce	0.145	−6.383	1.130	0.322
se	−2.648	−2.202	4.518	4.652

5. Conclusion

A robust DOB framework is proposed for a hybrid gantry stage with actuator asymmetry and payload-dependent LPV dynamics. Frequency-domain RGA and CPD are employed to assess coupling and to select a nominal model. Using the transform identified from the no-load condition, a unified representation is constructed, and robust stability is validated using experimentally measured FRFs across payload cases within the selected DOB bandwidth.

Future work includes closed-loop validation with an outer feedback controller and robustness evaluation under stronger unmodeled dynamics and continuously varying payload conditions.

CRediT authorship contribution statement

Hanul Jung: Writing – review & editing, Writing – original draft, Visualization, Validation, Software, Methodology, Investigation, Funding acquisition, Formal analysis, Data curation. **Jegwon Yoon:** Writing – review & editing, Validation, Resources, Methodology, Investigation, Formal analysis, Conceptualization. **Taejune Kong:** Writing – review & editing, Methodology, Investigation, Formal analysis. **Sehoon Oh:** Writing – review & editing, Supervision, Project administration, Methodology, Investigation, Conceptualization.

Declaration of competing interest

The authors declare that they have no known competing financial interests or personal relationships that could have appeared to influence the work reported in this paper.

Data availability

Data will be made available on request.

References

[1] Butler H. Position control in lithographic equipment [applications of control]. IEEE Control Syst Mag 2011;31(5):28–47.
[2] Tsai M-C, Hsieh M-F, Yao W-S. Synchronous control of linear servo systems for CNC machine tools. In: 2003 European control conference. IEEE; 2003, p. 2339–44.
[3] Mavinkurve UK, Tafrishi SA, Kanada A, Yamamoto M. An energy based control for vibration suppression in a rigid parallel series elastic actuator. In: 2021 IEEE/sICE international symposium on system integration. IEEE; 2021, p. 600–5.
[4] Wang W, Ma J, Cheng Z, Li X, de Silva CW, Lee TH. Global iterative sliding mode control of an industrial biaxial gantry system for contouring motion tasks. IEEE/ASME Trans Mechatronics 2021;27(3):1617–28.
[5] Bloemers T, Oomen T, Tóth R. Frequency response data-driven LPV controller synthesis for MIMO systems. IEEE Control Syst Lett 2021;6:2264–9.
[6] Heydari R, Farrokhi M. Robust tube-based model predictive control of LPV systems subject to adjustable additive disturbance set. Automatica 2021;129:109672.
[7] Bujarbaruah M, Rosolia U, Stürz YR, Zhang X, Borrelli F. Robust MPC for LPV systems via a novel optimization-based constraint tightening. Automatica 2022;143:110459.
[8] Cheng J, Wu M, Wu F, Lu C, Chen X, Cao W. Modeling and control of drill-string system with stick-slip vibrations using LPV technique. IEEE Trans Control Syst Technol 2020;29(2):718–30.
[9] Bloemers T, Oomen T, Tóth R. Frequency response data-based LPV controller synthesis applied to a control moment gyroscope. IEEE Trans Control Syst Technol 2022;30(6):2734–42.
[10] Skogestad S, Postlethwaite I. Multivariable feedback control: analysis and design. john Wiley & Sons; 2005.
[11] Yoon J, Kong T, Jung H, Oh S. Data-driven system decoupling algorithm with transfer function decoupling matrix. In: IECON 2023-49th annual conference of the IEEE industrial electronics society. IEEE; 2023, p. 1–6.
[12] Nozaki T, Mizoguchi T, Ohnishi K. Decoupling strategy for position and force control based on modal space disturbance observer. IEEE Trans Ind Electron 2013;61(2):1022–32.
[13] Stoev J, Ertveldt J, Oomen T, Schoukens J. Tensor methods for MIMO decoupling and control design using frequency response functions. Mechatronics 2017;45:71–81.
[14] Sariyildiz E, Oboe R, Ohnishi K. Disturbance observer-based robust control and its applications: 35th anniversary overview. IEEE Trans Ind Electron 2019;67(3):2042–53.
[15] Vafamand N, Arefi MM, Asemani MH, Dragičević T. Decentralized robust disturbance-observer based LFC of interconnected systems. IEEE Trans Ind Electron 2021;69(5):4814–23.
[16] Chen C-S, Chen S-K, Chen L-Y. Disturbance observer-based modeling and parameter identification for synchronous dual-drive ball screw gantry stage. IEEE/ASME Trans Mechatronics 2019;24(6):2839–49.
[17] Klauser E, Karimi A. Data-driven LPV control for harmonic disturbance rejection in a hybrid isolation platform. IEEE Trans Control Syst Technol 2025.
[18] Jung H, Kim W, Oh S. Data-driven dynamics decomposition of dual-drive gantry stage and robust decoupling control. IEEE/ASME Trans Mechatronics 2025.
[19] Park Y, Paine N, Oh S. Development of force observer in series elastic actuator for dynamic control. IEEE Trans Ind Electron 2017;65(3):2398–407.